

Small animal simultaneous PET/MRI: initial experiences in a 9.4 T microMRI

This article has been downloaded from IOPscience. Please scroll down to see the full text article.

2011 Phys. Med. Biol. 56 2459

(<http://iopscience.iop.org/0031-9155/56/8/009>)

View [the table of contents for this issue](#), or go to the [journal homepage](#) for more

Download details:

IP Address: 130.199.3.165

The article was downloaded on 10/05/2011 at 01:43

Please note that [terms and conditions apply](#).

Small animal simultaneous PET/MRI: initial experiences in a 9.4 T microMRI

Sri Harsha Maramraju¹, S David Smith², Sachin S Junnarkar³, Daniela Schulz², Sean Stoll⁴, Bosky Ravindranath¹, Martin L Purschke⁴, Sergio Rescia³, Sudeepti Southekal⁵, Jean-François Pratte⁶, Paul Vaska^{1,2}, Craig L Woody⁴ and David J Schlyer^{1,2}

¹ Department of Biomedical Engineering, Stony Brook University, Stony Brook, NY, USA

² Medical Department, Brookhaven National Laboratory, Upton, NY, USA

³ Instrumentation Division, Brookhaven National Laboratory, Upton, NY, USA

⁴ Physics Department, Brookhaven National Laboratory, Upton, NY, USA

⁵ Brigham & Women's Hospital, Boston, MA, USA

⁶ Université de Sherbrooke, Sherbrooke, Québec, Canada

E-mail: schlyer@bnl.gov

Received 29 September 2010, in final form 22 February 2011

Published 25 March 2011

Online at stacks.iop.org/PMB/56/2459

Abstract

We developed a non-magnetic positron-emission tomography (PET) device based on the rat conscious animal PET that operates in a small-animal magnetic resonance imaging (MRI) scanner, thereby enabling us to carry out simultaneous PET/MRI studies. The PET detector comprises 12 detector blocks, each being a 4×8 array of lutetium oxyorthosilicate crystals ($2.22 \times 2.22 \times 5 \text{ mm}^3$) coupled to a matching non-magnetic avalanche photodiode array. The detector blocks, housed in a plastic case, form a 38 mm inner diameter ring with an 18 mm axial extent. Custom-built MRI coils fit inside the positron-emission tomography (PET) device, operating in transceiver mode. The PET insert is integrated with a Bruker 9.4 T 210 mm clear-bore diameter MRI scanner. We acquired simultaneous PET/MR images of phantoms, of *in vivo* rat brain, and of cardiac-gated mouse heart using [¹¹C]raclopride and 2-deoxy-2-[¹⁸F]fluoro-D-glucose PET radiotracers. There was minor interference between the PET electronics and the MRI during simultaneous operation, and small effects on the signal-to-noise ratio in the MR images in the presence of the PET, but no noticeable visual artifacts. Gradient echo and high-duty-cycle spin echo radio frequency (RF) pulses resulted in a 7% and a 28% loss in PET counts, respectively, due to high PET counts during the RF pulses that had to be gated out. The calibration of the activity concentration of PET data during MR pulsing is reproducible within less than 6%. Our initial results demonstrate the feasibility of performing simultaneous PET and MRI studies in adult rats and mice using the same PET insert in a small-bore 9.4 T MRI.

(Some figures in this article are in colour only in the electronic version)

1. Introduction

Integrating positron emission tomography (PET) with magnetic resonance imaging (MRI) in research on small animals affords the opportunity for obtaining simultaneously structural and functional information. This unique confluence of these two distinct imaging modalities promises to support better diagnostic interpretation in hybrid imaging. Although PET combined with x-ray computed tomography (CT) scanners improved the accuracy in detecting diseased conditions in clinical and pre-clinical settings, a few shortcomings were identified (Mawlawi *et al* 2006, Sureshbabu and Mawlawi 2005). Compared to CT, MRI provides better soft-tissue contrast without the additional radiation dose (Huang *et al* 2009). MRI also extracts spectroscopic information via magnetic resonance spectroscopy (MRS) that measures pathological processes in organs, or ratios of metabolite concentrations to detect tissue-specific abnormalities. It can also be employed to assess functional phenotypes in transgenic mouse models (Tkac *et al* 2004). Combining this metabolic information from MRS with biochemical and molecular data from PET serves as a research tool and for monitoring disease progression in animal models. Another advantage of combining MRI, rather than CT, with PET is the ability to use different MR pulse sequences (e.g., gradient echo, spin echo) that offer a wide range of contrast mechanisms, like different relaxation times (soft-tissue contrast), flow, perfusion and diffusion. In addition, functional MRI (fMRI) yields functional information on the brain using blood oxygenated level-dependent (BOLD) contrast. Unlike sequential PET/CT procedures, the simultaneous acquisition of PET and MR images supports accurate spatial and temporal correlations.

Photomultiplier tubes (PMTs), the basis of conventional PET detectors, are very sensitive to high magnetic fields, so proving one of the main challenges in developing a PET/MRI scanner. Strong magnetic fields deflect the electrons' path between the dynodes in the PMTs, causing them eventually to lose their ability to detect light photons, thereby corrupting the PET data. Another hindrance is in placing the bulky PMT-based PET detector in the limited space inside the bore of the MR scanner. Mechanically integrating the PET detector hardware inside the MRI scanner is extremely difficult due to the size of the PMTs. The magnetic components often used in PET detectors cause inhomogeneities in the field, generating susceptibility artifacts and loss of quality in the MR images. The gradient fields may induce eddy currents due to the presence of ferromagnetic components in the PET scanner and the conductive materials that are shielding the radio frequency (RF) may distort the images. Therefore, only by minimizing electromagnetic interference (EMI) can we integrate the two scanners without compromising the performance of either one.

Solutions to this problem include moving the PMT-based detector modules outside the magnetic field, and employing fairly long optical light guides coupled to the scintillation detectors (Shao *et al* 1997, Garlick *et al* 1997, Slates *et al* 1999, Mackewn *et al* 2005, Raylman *et al* 2006, Imaizumi *et al* 2009, Yamamoto *et al* 2010). In this arrangement, the PMTs do not require EMI shielding and this configuration is relatively easy to implement. Novel PET/MRI approaches, such as the split-magnet design (Lucas *et al* 2006, Poole *et al* 2009) and the field-cycled MRI technique (Gilbert *et al* 2006, Bindseil *et al* 2011), also deliver usable PET/MRI data using PMTs. Although light guides minimized the EMI and gave good MRI signals, reportedly the performance of PMT-based PET devices was compromised because of significant loss of scintillation light. This configuration also may limit the PET scanner's axial field-of-view. Accordingly, this led to the development of solid-state PET detectors wherein the PET inserts can be placed in smaller bore magnets. Unlike the PMTs, small compact solid-state avalanche photodiodes (APDs) can operate in high magnetic fields (Pichler *et al* 2006, Grazioso *et al* 2006). They have higher quantum efficiency than PMTs

and can be coupled to the scintillators without needing optical fibers. New PET/MRI systems designed with APDs successfully gave simultaneous PET/MRI data from phantoms and mice (Judenhofer *et al* 2007, Judenhofer *et al* 2008, Catana *et al* 2006, 2008, Buscher *et al* 2010). The PET/MRI technology was extended to studies of human brains, with the PET detector mounted in a clinical 3 T human MRI scanner (Schlemmer *et al* 2008, Boss *et al* 2010b); a recent publication reported the feasibility of using it to diagnose intracranial tumors (Boss *et al* 2010a). In comparison to PMTs, the APD-based PET detectors have many advantages. Nevertheless, they may introduce subtle artifacts as the gain and noise in them are sensitive to temperature (Pichler *et al* 2006). A new development in solid-state photosensors using silicon photomultipliers (SiPMs) gives them the potential for use as PET detectors. With the strengths of both PMTs and APDs, they provide much higher signal-amplitudes than APDs, can be operated with simple preamplifiers, and are insensitive to magnetic fields. Currently, SiPMs are undergoing evaluations to establish their overall optimum performance for PET applications, including time-of-flight (Schaart *et al* 2010) and for their use in PET scanners operating in high magnetic fields (Hawkes *et al* 2007, McElroy *et al* 2007, Seong Jong *et al* 2008, España *et al* 2010, Kang *et al* 2010).

Here, we report our development of an MRI-compatible PET system, based on the rat conscious animal PET (RatCAP) detector (Vaska *et al* 2004, Schlyer *et al* 2004, Woody *et al* 2007b). We made the PET detector MRI compatible by using non-magnetic components in the detector's electronics. Previously, we reported preliminary PET/MRI data from scanning rats' brains (Schlyer *et al* 2007, Woody *et al* 2007a) in the Varian INOVA 4 T human MRI scanner using an MRI-compatible RatCAP. In this paper, we present our initial simultaneous PET/MRI results acquired in a high field 9.4 T microMRI scanner. We realized significant benefits by acquiring images in MRI scanners at higher field strengths because higher nuclear magnetization of the proton spins improve the signal-to-noise ratio (SNR). Furthermore, the BOLD effect increases with the strength of the static magnetic field (Gati *et al* 1997). With higher fields, we can define anatomical structures with better spatial resolution, so improving small-animal imaging wherein small lesions can be visualized, and different metabolites resolved with MRS. We aim to use these advantages to obtain good-quality PET/MRI rodent data in a 9.4 T MRI. However, with increasing field strengths, many technical limitations arise, such as inhomogeneities in the field and susceptibility artifacts (Toi *et al* 2010), making it challenging to maintain homogeneous fields in the imaged object. This is because even non-ferromagnetic materials can have a significant impact at high field strengths due to different susceptibilities of the material and the remaining unfilled space. As the MRI resonance frequency increases with rising field strength, the RF pulse wavelength declines, so that when it becomes similar to the dimensions of the object, it engenders dielectric effects. In human applications wherein the RF wavelengths are shorter than the head or torso, signal variations are enhanced due to irregular flip angles and non-uniformities in the field (Schick 2005). Another concern is the deposition of RF power in the tissues at higher field strength causing excessive heat. Nevertheless, these high-field strength limitations are not a problem for small animal MR imaging as the imaging object is quite small. Dedicated MRI coils achieve acceptable parameters at high fields (Doty *et al* 2007).

Similar to some other prototype MRI-compatible PET inserts, our PET detector uses APDs but differs significantly from other designs. We employ one-to-one coupling between the scintillator and APD; other approaches use light-sharing or charge-sharing technology (Pichler *et al* 2006, Catana *et al* 2006). The one-to-one coupling eliminates any dependence of the event positioning on the APD's gain shifts resulting from variations in temperature or supply voltage. However, it requires handling many electronic channels. To satisfy this requirement, we developed a 32-channel mixed-signal application-specific integrated circuit

(ASIC) to multiplex the data into one output line (Pratte *et al* 2008). The ASIC resides close to the detector to reduce cabling requirements and minimize stray capacitance at the preamplifier input. In contrast, other approaches place the front-end electronics as far as possible from the imaging field to reduce potential EMI. Importantly, each ASIC consumes only 117 mW of power, only natural convection is required for cooling. The small footprint of the ASIC and its high degree of multiplexing yield a highly compact system that efficiently uses the limited space within the MRI bore. While our the field-of-view (FOV) is similar to the other small animal PET/MRI prototypes, our PET insert (80 mm outer diameter (OD)) and custom-built MRI coil (32 mm inner diameter (ID)) are much smaller than other PET inserts optimized for 7 T MRI scanners (Catana *et al* 2006, Judenhofer *et al* 2008), and use larger MRI coils.

A second significant difference is in the shielding from EMI (Catana *et al* 2006, Pichler *et al* 2006, Wu *et al* 2009, Wehrl *et al* 2010); we do not shield the PET system, leaving it sensitive to radio-frequency (RF) pulse sequences. We are considering using shielding but because the system's performance depends partly upon the shield's final configuration, we cannot present detailed performance results; rather, we discuss our initial findings that demonstrate the feasibility and potential hurdles of using our approach. In summary, our methodology has important differences from contemporary PET/MRI systems, and this report evidences its feasibility.

2. Methods

2.1. MRI-compatible RatCAP PET detector

The RatCAP detector (Woody *et al* 2007b) is a three-dimensional (3D) ring tomograph for imaging the brain of a conscious adult rat. We directly attach this miniaturized PET device to the rat's head to eliminate motion between its head and the scanner, while allowing the rat to move (Vaska *et al* 2004). Retaining the same design, architecture, and technology, we used the latest version of the RatCAP with non-magnetic materials (such as APD sockets, pins) to integrate the PET detector, optimized for reliable operation in the presence of high magnetic fields. A significant advantage in our PET system is the implementation of low-voltage differential signal (LVDS) readout that minimizes potential digital interference on analog circuits. Unlike the RatCAP, the PET system is no longer attached to the rat's head. The front-end readout (Pratte *et al* 2008), signal-processing chain (Junnarkar *et al* 2008), PET data processing (Park *et al* 2008) and image reconstruction (Southechal *et al* 2007) of the new version of the RatCAP (Vaska *et al* 2007) are detailed elsewhere. Briefly, 12 detector blocks constitute the PET ring, each block consisting of a 4×8 array of $2.22 \times 2.22 \times 5$ mm³ lutetium oxyorthosilicate (LSO) crystals (Proteus Inc.) bonded together with a 0.078 mm thin reflective foil (3M VM 2000), separating individual crystals. The LSO crystals are coupled to a matching non-magnetic S8550 (Hamamatsu) APD array (figure 1(a)). Others reported experimental measurements and simulations of the efficiency of light collection by these APD arrays (Kriplani *et al* 2003). Vaska *et al* (2004) and Woody *et al* (2004) published preliminary results using a 5 mm LSO crystal block coupled to the S8550 APD array. Figure 1(b) depicts each LSO-APD block plugged into a non-magnetic APD socket mounted on the flexible printed circuit board (PCB). The flexible PCB, rolled up and secured in a plastic housing, forms eight 48-crystal PET rings with 384 crystals, having a transaxial FOV of 38 mm and an axial extent of 18 mm.

The front-end electronics include the 32-channel ASIC. Each channel has a charge-sensitive preamplifier (CSP); a 5-bit programmable gain in the pole-zero network compensating for the spread in light collection efficiency; third-order bipolar Gaussian shaper

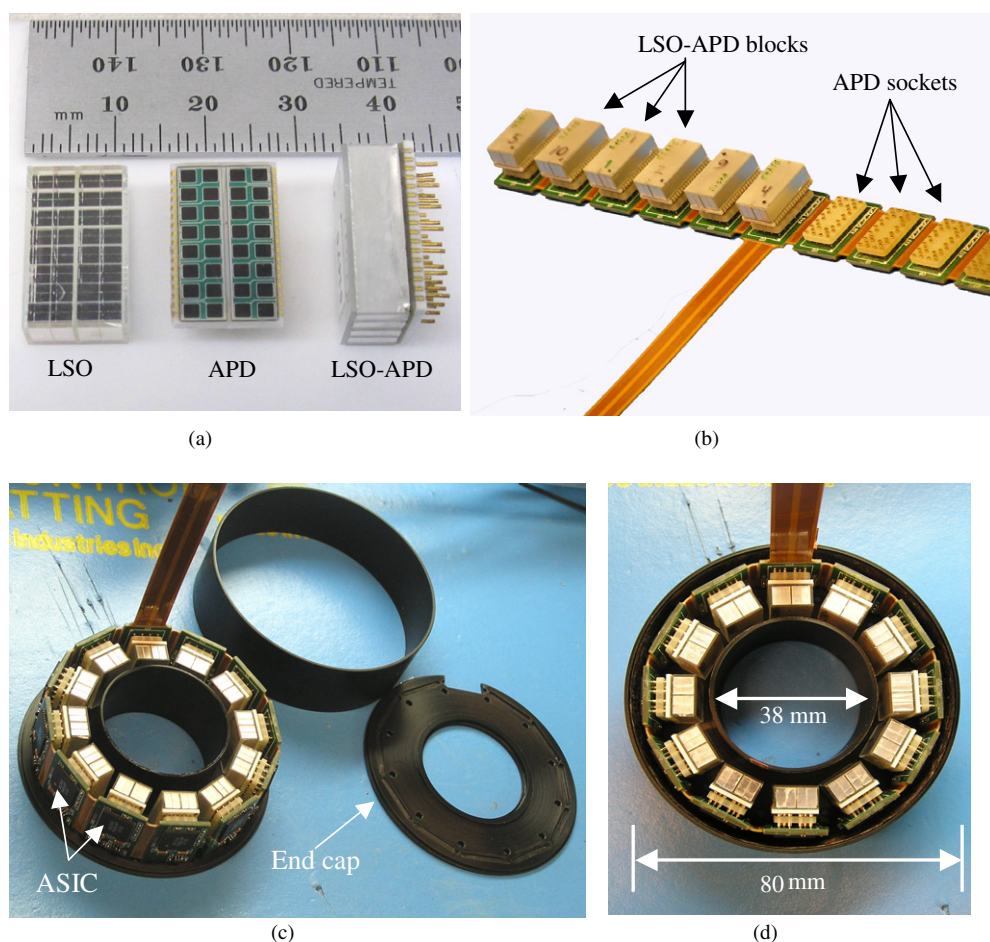


Figure 1. (a) LSO crystals and non-magnetic APDs. (b) The LSO-APD blocks are coupled and plugged into the non-magnetic APD sockets on the flexible circuit. (c) Custom-designed ASICs are embedded at the front-end of the PCB. (d) The flexible PCB is rolled to form the PET ring in a plastic housing.

with a peaking time of 80 ns; and two energy arming comparators and a zero-cross comparator. In order to minimize interconnects between the detector front-end and readout electronics, a 32-to-1 serial priority encoder is embedded in the ASIC, which multiplexes timing information and the crystal address of every event through the LVDS digital output. Serialized timing and address information from the ASIC is received and processed on a stand-alone electronic board called the time-to-digital converter and signal-processing module (TSPM). The TSPM consists of an Altera Stratix II field programmable gate array (FPGA)-based 12-channel time-to-digital converter (TDC) where each received PET event is time-stamped with timing and position information for readout (Junnarkar *et al* 2008). The digital-to-analog converters (DACs) on the TSPM board allow programming of the lower- and upper-energy discriminator thresholds so the thresholds can be set in a two-energy gating window mode. The TDC module can reach a resolution of 625 ps. The time-stamped PET events are encoded into a 64-bit word (43-bit absolute time stamp; 4-bit block identification; 6-bit fine time stamps; 5-bit

crystal identification and the remaining are the spare bits). Gigabit serializer (HDMP-1022 Agilent Technology) transmits the 64-bit word events via optical transmitters. These standard connector (SC)-type optical transceivers retain the signal integrity in higher magnetic fields. The data is transferred via optical fibers to an external peripheral component interconnect (PCI)-based data acquisition board (Junnarkar *et al* 2008). The PET detector has a system clock of 100 MHz on the TSPM board that is daisy-chained to all the 12 ASICs embedded on the flexible circuit. When operating the magnet, the PET system clock interferes with multi-harmonic resonances of the MRI's proton frequency (400 MHz). Therefore, we modified the system clock oscillator from 100 to 106 MHz that resulted in shifting any of the possible RF interference or spike patterns entirely out of MR imaging bandwidth, thereby eliminating any line artifacts in the MR images caused by the presence of powered PET electronics. All the state machines of the PET detector electronics chain are synchronized with the PET system clock. The +6 V dc power supply (Matsusada) powers the system clock. A bias voltage of approximately 420 V, supplied by high-voltage dc power supplies (Keithley Instruments, model no 6487), powers the APDs. A single shielded cable carries the low voltage and high voltage dc lines, along with a central common ground, from the power supplies to the PET detector. The shielded cable arrangement helps in minimizing the area of the ground loops in the cables, thereby minimizing EMI.

PET data were acquired, in a list-mode format, on Windows XP using the LabVIEW interface and were written directly to disk. Data are processed offline using a 3D maximum likelihood-expectation maximization (ML-EM) iterative algorithm to reconstruct the PET images (Southehal *et al* 2007). Using the Monte Carlo SIMSET simulation (Lewellen *et al* 1998) system response matrix, the PET detector's FOV is divided into $0.9581 \times 0.9581 \times 1.149$ mm³ voxels. The images were visualized using acquisition sinogram and image processing (ASIPro) VM microPET analysis software (Concorde Microsystems). The PET data from the phantom and animal studies were reconstructed for 50 to 100 iterations, depending on the imaging sample being reconstructed; they were post-smoothed using a 3D Gaussian filter ranging between 1.5 and 1.8 mm full-width-at-half-maximum (FWHM). The individual crystals' dimensions (2.22 mm) limit the system's spatial resolution. The reconstructed image resolution is 1.2 mm FWHM at the center of the FOV, and under 2 mm FWHM toward its edge (Southehal 2009). The PET image generates 33×33 voxels transaxially, and 17 voxels axially (slice thickness of 1.05 mm). The overall system's energy resolution is 13%, coincidence timing resolution is 10 ns, and system sensitivity at the center of FOV is 0.3% (Southehal 2009).

2.2. Design of the MRI coil for PET/MRI studies in 9.4 T

A standard Bruker MRI birdcage coil, routinely used for imaging studies at 9.4 T, has an ID of 72 mm. It was impractical for simultaneous PET/MRI measurements considering the geometric design of the PET detector (ID/OD = 38 mm/80 mm). Therefore, we fabricated custom-designed volume coils in-house that fit inside the detector (figure 2). The ID/OD of the MRI coil is 32 mm/37 mm and the coil is 76 mm long, with an active axial extent of 27.4 mm. Although the geometry of the PET detector ring limits the imaging volume, it is large enough to center an adult rat's head inside the coil's active region. The coil is composed of two pairs of cross-connected hexagonal coils with thin strips of copper, mounted on a cylindrical structure made of G10 plastic material. Operating in a transceiver mode, we tune the coil to its proton resonance frequency of 400 MHz using non-magnetic fixed and variable-trimmer capacitors (Voltronics Corporation, NJ) connected to the tuning rods. We inserted it into the PET detector ring, aligning the PET- and MR-imaging volumes with each other mechanically

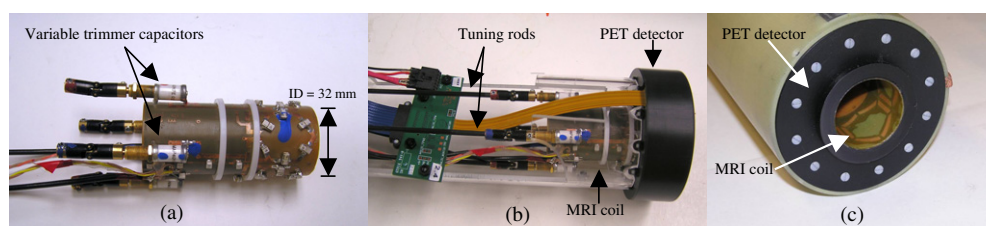


Figure 2. (a) Custom-built MRI coil alone, (b) and (c) secured inside the PET device and housed in a black plastic casing.

to obtain accurate co-registration. Inside the detector, the coil is secured in the X , Y , and Z directions with non-metallic stoppers to avoid its rotation.

2.3. The 9.4 tesla microMRI scanner and PET/MRI experimental setup

We are using a Bruker 9.4 T superconducting horizontal bore magnet (Bruker Biospec 94/20, 400 MHz proton frequency, Magnex scientific) for the PET/MRI acquisitions that has a clear bore diameter of 210 mm. The Bruker Avance console controlling the scanner is equipped with an actively shielded 116 mm diameter gradient set (B-GA12) that can produce a maximum gradient strength of 200 mT m^{-1} . The MR images were acquired, reconstructed, displayed and analyzed using the ParaVision software from Bruker Biospin. The five Gauss fringe fields extend from the magnet's center 2 m radially and 3 m axially in either direction. The MR room is not a Faraday cage and we do not employ patch-panel filtering for the PET/MRI scans.

A long support tube (ID = 84 mm) made of G10 plastic material extends through the magnet's entire bore. Two concentric foam liners between the gradient set and the support tube suppress noise from mechanical vibrations, leaving 85 mm open access for imaging. The support tube is secured at both ends of the magnet, and can accommodate two tube assemblies made of G10 plastic material (figure 3). The first tube assembly secures the MRI coil inside the PET detector and guides its data cables from the rear end of the magnet's bore. The cables are connected to the TSPM board secured in a metal enclosure, as shown in figure 3(a). The second tube assembly is used to position the animal on the animal-handling platform and is then guided from the front end of the magnet bore, so to align the region of interest of the animal and the PET detector in the homogeneous region of the magnetic field.

This arrangement helps in abutting and detaching the tubes independent of the PET electronics and is convenient for positioning the animal and administering the radiotracer. All PET dc-power supplies are well outside the MRI room during the scans. Figure 4 is a schematic of the PET/MRI setup in the 9.4 T magnet.

2.4. Effect of PET on MR images

To test the effect of the PET detector on the MR image quality, a cylindrical phantom (ID = 17 mm) filled with a 2.5 g L^{-1} of a gelling agent (Gelzan), was placed inside the MRI coil. The MRI data was acquired with no PET detector, with PET detector powered-off and with the PET detector powered-on, respectively; using the rapid acquisition with relaxation enhancement (RARE) fast spin echo sequence, and the fast low-angle shot (FLASH) gradient echo sequence. There is one 90° pulse followed by eight 180° pulses in this RARE sequence (the rare factor is 8). Table 1 shows the MR scan sequence parameters. These MR images were

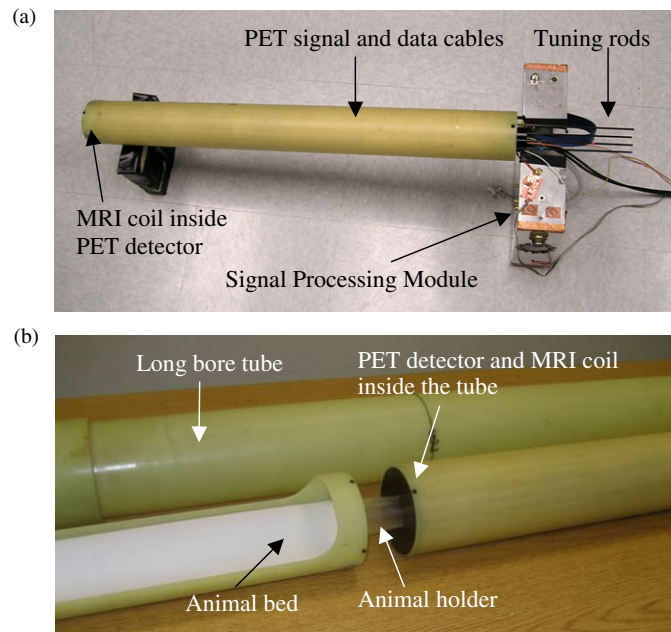


Figure 3. (a) The MRI coil and PET detector are secured in a G10 plastic tube assembly. The data and power cables, along with the signal processing module, remain at the rear end of the magnet. (b) A second tube assembly with the animal bed positions, the animal and slides into the first tube. A long bore support tube accommodates both tube assemblies inside the magnet.

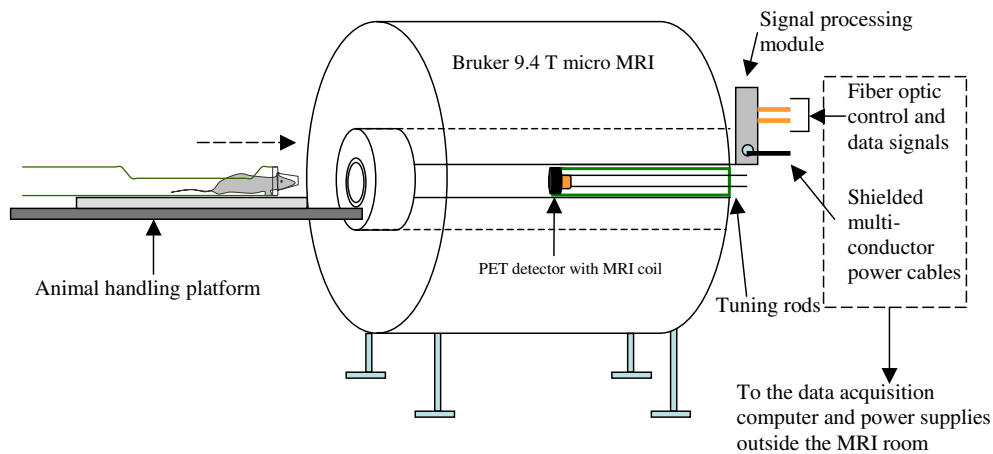


Figure 4. Schematic of a PET/MRI acquisition setup in a 9.4 T Bruker Biospin microMRI scanner. We sited the MRI coil secured inside the PET detector in the magnet's isocenter. The animal for imaging is positioned on the animal handling platform that is slid in from the front of the magnet abutting the tube encapsulated by the PET detector and the MRI coil.

Table 1. MRI scanning parameters for SNR phantom measurements.

Sequence	Field-of-view (mm ²)	Matrix size	Repetition time, TR (ms)	Echo time, TE (ms)	Slice thickness (mm)	Flip angle (°)
RARE spin echo	83.9 × 167.8	512 × 1024	3753	60	0.85	180
FLASH gradient echo	83.9 × 167.8	512 × 1024	327	3.9	0.85	15

acquired after setting a maximum receiver bandwidth of 900 kHz allowable around the MRI's center frequency, to observe the extent of any possible RF interference due to the presence of PET electronics. The SNR was measured with the ImageJ MR image processing tool. We placed a small region-of-interest (ROI) on the phantom and a second one in the background outside the phantom across all planes to measure, respectively, the signal and noise values. We computed the SNR for each PET condition by averaging the ratio of mean pixel intensities and standard deviation across all slices. To evaluate the noise contribution in MR images due to the PET electronics, two sequential MR scans were acquired with the same MR scanning protocols when PET was powered-off. A difference image of the two sequential scans was then compared with the difference image acquired when PET was powered-on.

To investigate the impact of the PET detector on the homogeneity of the static magnetic field (B_0), we generated field maps using a uniform cylindrical phantom (ID = 28 mm) filled with 1 g L⁻¹ CuSO₄ solution. We first mapped the variations in B_0 homogeneity with all the shim adjustments set to zero (TR/TE = 20 ms/1.5 ms; FOV = 32 × 32 mm²; matrix size = 64 × 64; pixel size = 0.5 mm). We then shimmed the field using the MAPSHIM protocol in the Bruker ParaVision 5.0 software. In our study, we chose the isotropic 3D 0.5 mm grid spacing for the measurement. The MAPSHIM protocol can calculate the optimal shim settings to maximize the field homogeneity over a limited volume within the imaging sample. The field maps were then acquired with and without shim adjustments for the powered PET condition using the same spatial location of the cylindrical phantom centered in the active imaging volumes of the custom-built MRI coil and the PET detector; the shim adjustments were optimized over a 17 × 17 × 17 mm³ volume on the phantom. The two-dimensional (2D) phase images of the cylindrical phantom were generated with the PET detector in FOV in radial (XY) and sagittal (XZ) planes. In addition, we drew contour lines on the field maps along XY and XZ directions for unshimmed and shimmed conditions with the PET detector in the FOV and compared them with the no-PET condition acquired using a standard Bruker birdcage coil (ID = 72 mm; OD = 112 mm). We plotted variations in the B_0 field before and after shimming along the center of the image planes with and without PET. This experiment gave a quantitative understanding of the extent of variation in B_0 homogeneity in the X , Y and Z directions caused by the detector.

2.5. Effect of the MRI on the PET detector

We employed gradient and RF-excitation pulses in the presence of the PET detector for acquiring data on the phantom data as described above. The effect on this PET data from each one was recorded independently by probing the analog output of a single PET channel with a digital oscilloscope (Tektronix TDS7254B). The statistics of the PET count rate were recorded for different RF-only and gradients-only acquisitions, and compared to the baseline counts to identify any interference on the PET list-mode data.

2.6. PET calibration of activity concentration

To calibrate the PET images during MRI acquisition, we used a uniform cylindrical phantom (ID = 28 mm) that fits inside the MRI coil. The phantom, filled completely with 1.1 MBq ml⁻¹ of 2-deoxy-2-[¹⁸F]fluoro-D-glucose (FDG), was carefully positioned in the active imaging regions of the MRI coil and the PET detector. We calibrated the radioactivity using aliquots of the solution, and a calibrated sodium-iodide well counter (Picker). To test the reproducibility of the quantitation, we acquired phantom PET data in the list-mode data during active RF-pulse excitation. This acquisition was repeated with the same MR parameters and the two datasets were reconstructed, using the ML-EM algorithm and post-smoothed. We drew a large ROI on each of the images of the cylindrical phantom (avoiding the edges) to obtain the mean values of radioactive concentration across all images. We assessed the calibration factors for each of the datasets by taking the ratio of the well-counter value to the ROI-measured value.

2.7. Preparation for rat brain studies

The Institutional Animal Care and Use Committee (IACUC) at Brookhaven National Laboratory (BNL) approved all the animal experiments: They were conducted in accordance with the *Guide for the Care and Use of Laboratory Animals*. Sprague-Dawley female rats (~260 g) were used for all the PET/MRI experiments in the 9.4 T MRI scanner. A Lucite holder supported the rat's head. The rats were anesthetized intraperitoneally with pentobarbital (Nembutal, 40 mg kg⁻¹) and given glycopyrolate (0.15 ml) and saline (1 ml) along with the anesthetic to control salivation and hydration, respectively. To maintain anesthesia while in the scanner, we exposed the animals to a gas mixture of isoflurane (up to 2%) and oxygen. Approximately, 22 MBq of [¹⁸F]-FDG radiotracer was administered intravenously through a jugular vein catheter to obtain the FDG distribution in the rat's brain. PET/MRI data were acquired 30 min post-injection. We acquired an *in vivo* ¹H MR spectrum of the rat brain whilst the PET was powered using a point-resolved spectroscopy (PRESS) sequence. The selection of the volume of interest (VOI) size and its localization centered at frontal cortex of the rat brain was based on the RARE sequence (TR/TE = 2000 ms/12 ms; 512 signal averages; acquisition time = 17 min 12 s) with a voxel size of 2 × 6 × 4 mm³. The echo planar imaging (EPI) sequence was acquired in the presence of the powered PET system (TR/TE = 1500 ms/19.2 ms; flip angle = 90°; FOV = 25.6 × 25.6 mm; matrix size = 128 × 128; slice thickness = 1.5 mm; acquisition time = 6 s). In another experiment, we administered approximately 29 MBq of [¹¹C]raclopride intravenously to assess dopamine D2 receptor availability in the rat's brain.

2.8. Preparation for cardiac mouse studies

We selected Swiss-Webster male mice (25–30 g) for our PET/MRI studies of the mouse heart, after replacing the rat's head holder on the animal platform with a customized mouse holder made of G10 plastic material. Physiological monitoring probes were connected to the mouse's forepaws and the holder was secured in the animal-tube assembly. The mice were anesthetized in the same manner as were the rats. Approximately 11 MBq of [¹⁸F]-FDG was injected through the tail vein and PET/MRI data were collected 30 min thereafter.

We scanned the animals with the attached physiological monitoring probes in place. We monitored and recorded their vital signs, i.e. pulse rate, respiratory rate, electrocardiogram (ECG), and body temperature (maintained at 37 °C), using an MRI-compatible small-animal monitoring system (SA Instruments, Stony Brook). With the ECG-gating technique, we

Table 2. MRI scanning protocols for simultaneous PET/MRI acquisition.

Parameter	Rat brain ^{18}F -[FDG]	Rat brain (^{11}C)		Mouse heart (^{18}F -[FDG])
Sequence	FLASH – 3D	RARE	FLASH – 3D	FLASH – 3D <i>Cine</i>
Matrix size	$256 \times 128 \times 128$	256×256	$256 \times 256 \times 256$	$86 \times 256 \times 860$
Time to echo, TE (ms)	3.4	39.4	3.4	2.7
Repetition time, TR (ms)	15	2500	15	10
Field-of-view ($\text{mm}^2 \text{mm}^{-3}$)	$51.2 \times 25.6 \times 25.6$	76.8×38.4	$38.4 \times 76.8 \times 38.4$	$42.8 \times 21.4 \times 21.4$
Slice thickness (mm)	0.2	0.9	0.15	0.167
Pixel size (mm)	0.2	0.15	0.15	0.249
Flip angle ($^\circ$)	15	180	15	10
Scan time	16 min 29 s	5 min 33 s	33 min	34 min 54 s

extracted the ten individual phases of the mouse's cardiac cycle. Each phase (R-R interval) is framed into 10 ms bins to obtain a dynamic MR image of the heart. The PET images also were R-wave-gated by synchronizing the data acquisition with the MRI-gating pulse. The transistor–transistor logic (TTL) input signal from the ECG gating device is directly fed into the PET signal-processing module (TSPM) that triggers the gating pulse in the PET list-mode data. The PET data was binned into ten 10 ms frames that are accurately co-registered with the MR image frames. Summing the data from each frame with the corresponding temporal frame form an image, yielding ten PET frames corresponding exactly in time with the ten MR frames.

The standard MR sequences included FLASH-gradient echo and RARE spin echo sequences. Table 2 lists the MRI scanning protocols for the animal scans. The PET and MR images were co-registered using the PMOD version 2.75 image fusion software. The MR image is loaded as a reference-study file. We selected an orthogonal layout to display all the planes. The PET image was loaded as a re-slice file and matched spatially with the MR reference file.

3. Results

3.1. Effect of PET on MR images

Figure 5 shows the MR images acquired with a much wider acquisition bandwidth of 900 kHz for each of the PET conditions, using the imaging sequences described in table 1. No noticeable visual artifacts were apparent on the phantom images. However, a line streak in phase encoding direction is faintly noticeable in all the MR images acquired for each of the PET conditions. The presence of the streak even in no-PET condition indicates the absence of any additional artifacts or RF interference on the MR images acquired with the PET detector in place. In addition, the line streak is well outside the conventional acquisition bandwidth settings of MR images. We observed that the difference image of the two sequential MR images shown in figure 5(a) acquired with the same MR parameters with PET powered-off is comparable to the difference image in figure 5(b) where one of the MR acquisitions is with PET powered-on. The difference image of no-PET versus PET powered-on condition

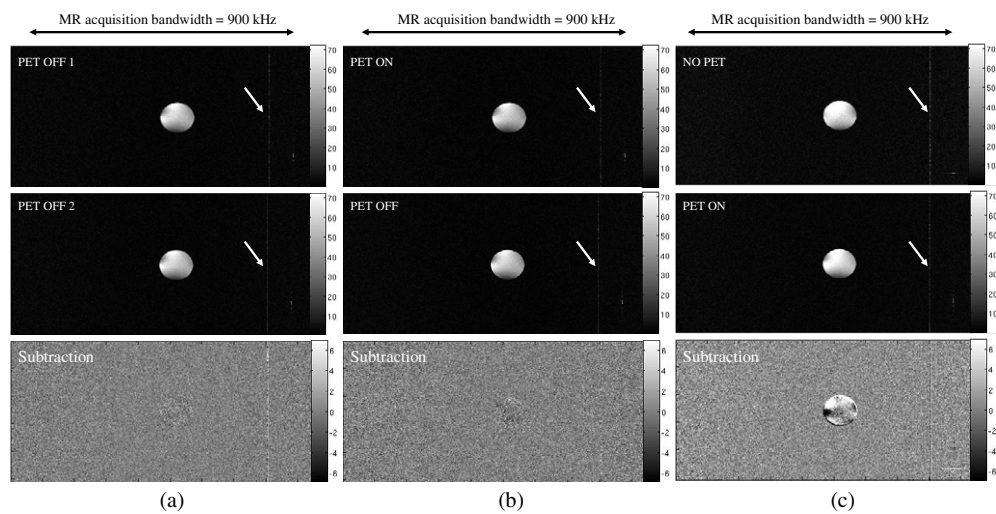


Figure 5. Column 1: (a) MR RARE spin echo phantom images and their normalized difference, of two sequential acquisitions with PET OFF condition with the same MR parameters. Column 2: (b) PET ON and PET OFF conditions, respectively, along with its difference image. Column 3: (c) NO-PET and PET ON conditions, respectively, along with its difference image. Arrows indicate faint line streaks. All the images were acquired across the maximum allowable bandwidth of 900 kHz with 512×1024 pixels in the image matrix.

Table 3. SNR^a of MR images for various PET conditions.

Parameter	No PET	PET OFF	PET ON
RARE	46.6 ± 3.7	43.5 ± 3.5	42.4 ± 3.8
FLASH	33 ± 2.7	32.8 ± 4	32.8 ± 4.5

^a SNR = Mean \pm standard deviation.

(figure 5(c)) shows the difference in signal intensities in the phantom. This could be a result of any displacement in phantom positioning, coil re-assembling and re-tuning with the PET detector that is bound to occur between the scans. However, there is no additional background noise contribution in the images. Since these observations are similar for MR images acquired with FLASH sequence, the results are not presented in the paper. Table 3 shows the SNR measurements for RARE and FLASH sequences for each of the PET conditions.

Figure 6 shows the field maps of the cylindrical phantom in the XY and XZ planes acquired in the presence of the PET detector before shimming. The contour lines spaced every 120 Hz (0.3 ppm) were overlaid on the field maps and were compared with no-shim (figures 6(a) and (b)) and with shimming conditions (figures 6(d) and (e)). Figures 6(c) and (f) show the variation in the B_0 field along the central line without and with shim adjustments, respectively. Figure 7 shows the same analysis but without the PET detector. The maps acquired without the detector are similar to those shown in figure 6 but show less variation over the phantom's volume. The phantom was placed 2 mm below the magnet's isocenter for the maps shown in figure 7, resulting in the lack of concentricity for the contour lines within the phantom's volume. The conclusion we drew from these data is that the presence of the PET detector had a significant impact on B_0 homogeneity, but well within the range of adjustment of the shim coils.

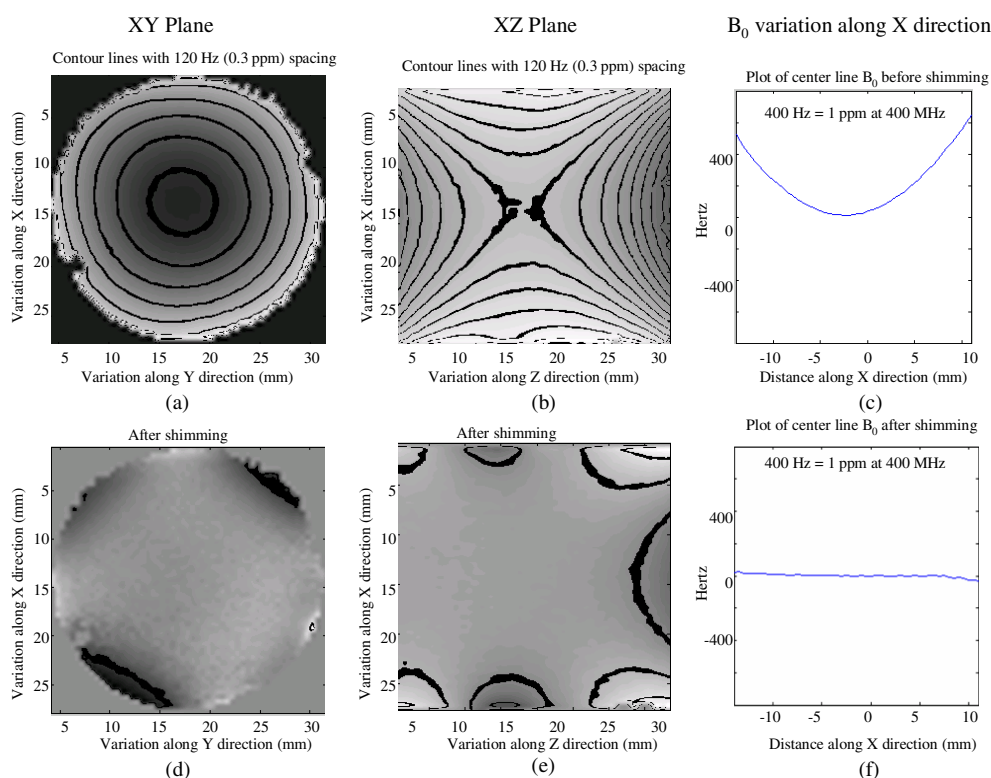


Figure 6. Field maps with contour lines overlaid in the presence of PET in MR FOV. (a)–(c) Before shim adjustments; (d)–(f) after shim adjustments.

3.2. Effect of MRI on the PET detector

When the gradients were applied individually (X , Y and Z) and all together, independent of the RF pulses, there was no change in the PET count rate. In addition, no degradation was evident in the shape of the analog output pulse of the PET signals from oscilloscope measurements. On the other hand, we noted spurious counts (seen as spikes in the count rate) in the list-mode PET data-stream during RF excitation. Figure 8 shows the list-mode data counts histogrammed into millisecond time-bins. Since the unshielded PET readout electronics are near the MRI coil, we believe that the strong RF excitation pulses interfere with the readout electronics that then appear as spurious spikes in the PET list-mode data. However, evidently the PET readout reverts back to its normal acquisition-mode between RF pulses. We gated-out those time bins containing noisy RF spikes during our post-processing of the PET data, by setting an appropriate count-rate threshold above which we discarded the data acquired during the RF spikes; it revealed a dead time corresponding to the RF duty cycle of the sequence. For FLASH, sequences for example, the RF pulse-duration is 1 ms and the repetition time is 16 ms per slice; it entailed a loss of 6.25% of the PET counts after gating out the RF spikes. For RARE sequences with the rare factor 8, the values were 16% to 28%, depending on the duration of the RF pulse that ranged between 2 and 4 ms; it also depended on the number of slices acquired. Therefore, we discarded the PET data during the onset of the RF pulses

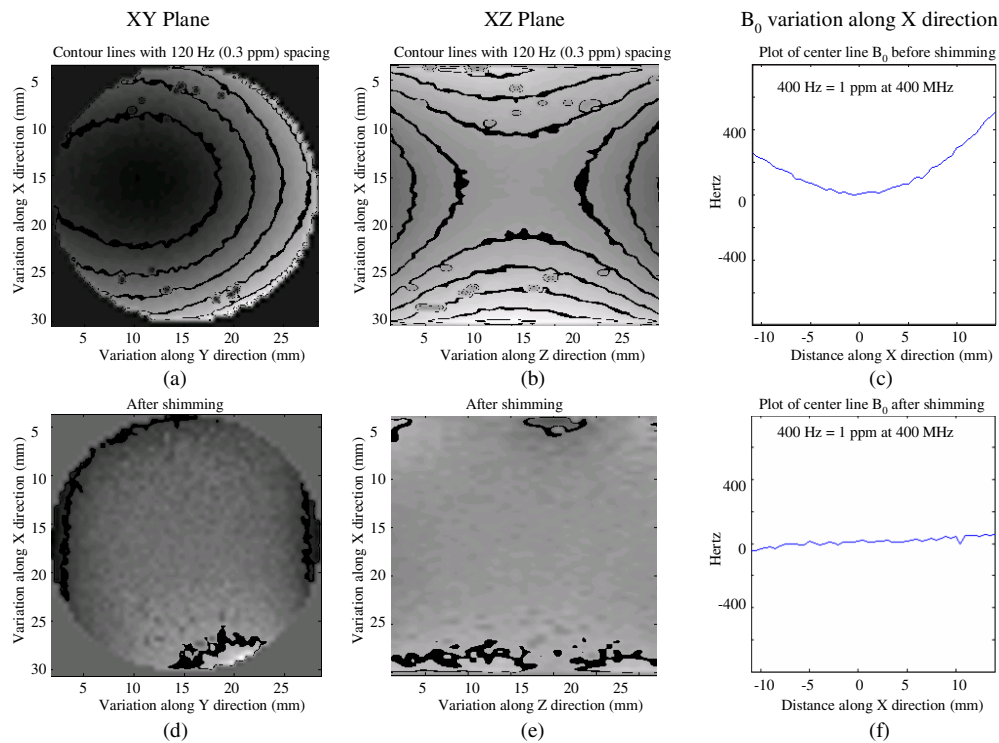


Figure 7. Field maps with contour lines overlaid in the absence of PET. (a)–(c) Before shim adjustments; (d)–(f) after shim adjustments.

irrespective of any flip angle or imaging sequence because the dead time in the PET data is due to the duty cycle of the RF alone.

3.3. PET calibration of activity concentration

With the FLASH MR pulsing during the PET acquisition, we gated out the noisy spikes in the PET data during offline processing, before reconstructing the image. We calibrated the uniform cylinder phantom from the two PET datasets by drawing ROIs on the post-smoothed reconstructed PET images. The measured calibration factors were repeatable within 6% after accounting for the gated-dead time, demonstrating the ability to acquire quantitative PET data during MR pulsing.

3.4. Simultaneous PET/MR images of the rat's brain and of the mouse heart

The MRI-, PET-, and co-registered images of the rat's brain acquired after injecting [^{18}F]-FDG show the glucose distribution in the brain (figure 9). The FDG localization is noticeable in the Harderian glands within the eye's orbit, and in different regions of the brain.

Figure 10(a) shows the *in vivo* ^1H MR spectrum of the rat brain's frontal cortex using the PRESS sequence. The inset shows the voxel selection on the cortex. Different metabolites, such as total creatine (tCr), total choline (tCh), glutamate (Glu), *N*-acetylaspartate (NAA), lactate (Lac), and lipids clearly are discernable when acquired in the presence of the powered

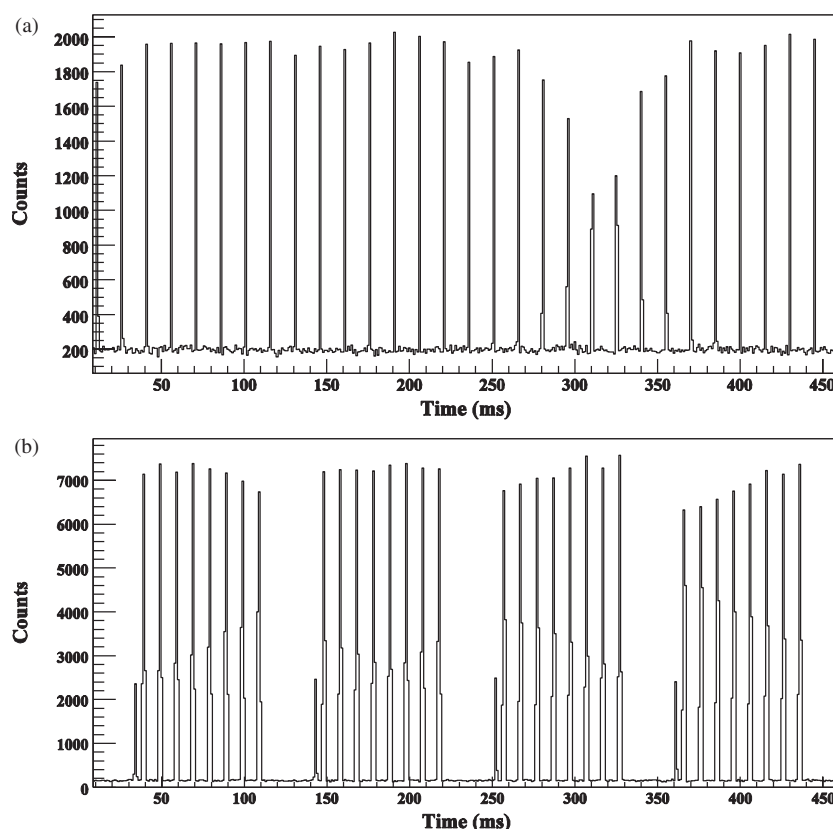


Figure 8. (a) Spurious counts seen as spikes in the list-mode PET data that correspond to the RF pulsing in (a) FLASH gradient echo sequence, and (b) RARE spin echo sequence with the spikes corresponding to one 90° pulse and eight 180° pulses. The magnitude of 90° spike is smaller than the 180° spikes.

PET detector. Figure 10(b) shows the three EPI transverse slices of the rat brain acquired in the presence of the powered PET detector. These images demonstrate the lack of significant degradation in field homogeneity or in eddy current effects because of the powered PET detector's presence.

The uptake of [^{11}C]raclopride, mainly in the striatum of an anesthetized rat brain, is shown in transverse and coronal views, respectively, in figures 11(a) and (b), using the different MRI pulse sequences listed in table 2. Figure 11(c) shows both the MRI and PET temporal frames of a ten-frame FLASH 3D *cine* MR sequence of a mouse's cardiac cycle.

4. Discussion

We demonstrated the feasibility of undertaking simultaneous PET/MRI studies using an MRI-compatible version of the RatCAP PET detector inside a 9.4 T MRI scanner. There was no additional noise contribution or RF interference in any of the MR images acquired with each of the different PET conditions, even after increasing the acquisition bandwidth by a factor of 6 compared to normal bandwidth settings. We followed appropriate grounding practices

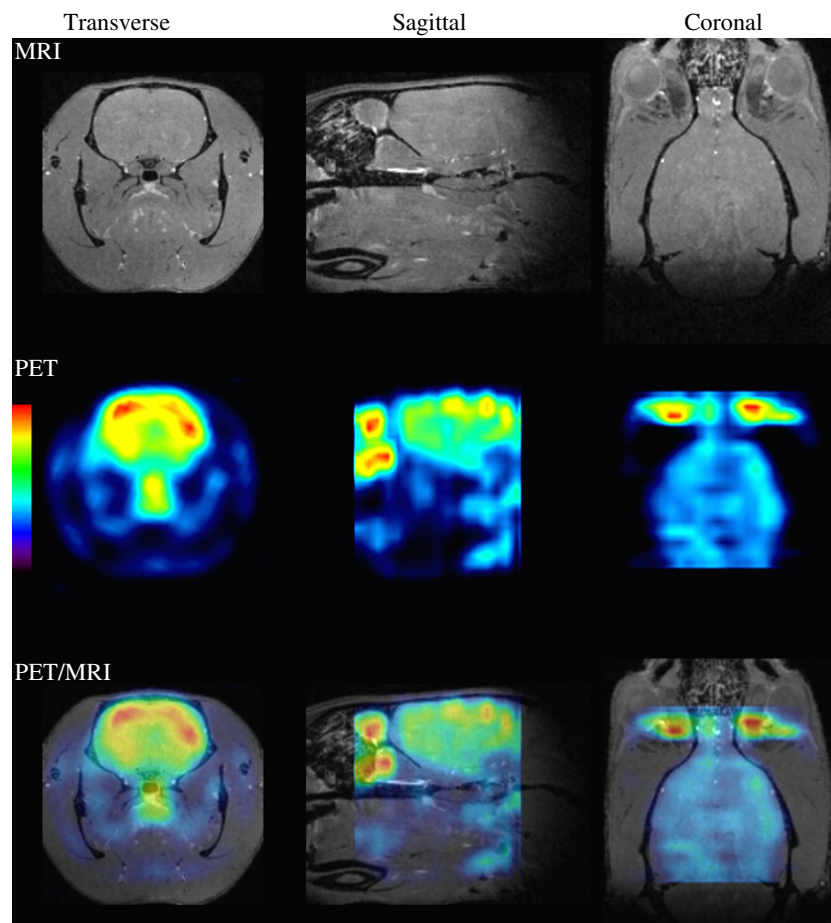


Figure 9. Simultaneous PET/MR images of a rat brain injected with [^{18}F]-FDG using the FLASH-3D isotropic MR pulse sequence (row 1: MR images; row 2: PET images; row 3: PET/MRI overlay) in transverse (column 1), sagittal (column 2) and coronal (column 3) views.

to minimize grounding loops by confining the PET power cables in a single multi-conductor shielded cable extending from the power supplies to the PET detector's tube assembly. In the presence of a powered PET detector, there was no significant degradation in the SNR measurable from the MR images acquired using RARE and FLASH sequences, compared to images acquired without the PET detector. Any slight drop in the SNR mainly could reflect the electromagnetic coupling of the MRI coil to the metallic components in the nearby PET detector. We cannot rule out subtle changes in the quality of the MR image due to re-assembling and re-tuning of the MRI coil, re-adjusting the phantom's positioning and load variations with the PET detector. Even in the absence of the PET detector, the SNR in the phantom images acquired using FLASH sequences was comparatively lower than in the RARE sequences as we expected, since the 180° echo-train pulses in the latter refocus the dephased proton spins (due to heterogeneities in the magnetic field), thereby increasing the signal. It also depends on the different relaxation times of the MRI agents used in the phantoms, and MR imaging sequence parameters. For example, the largest decrease in the SNR reportedly

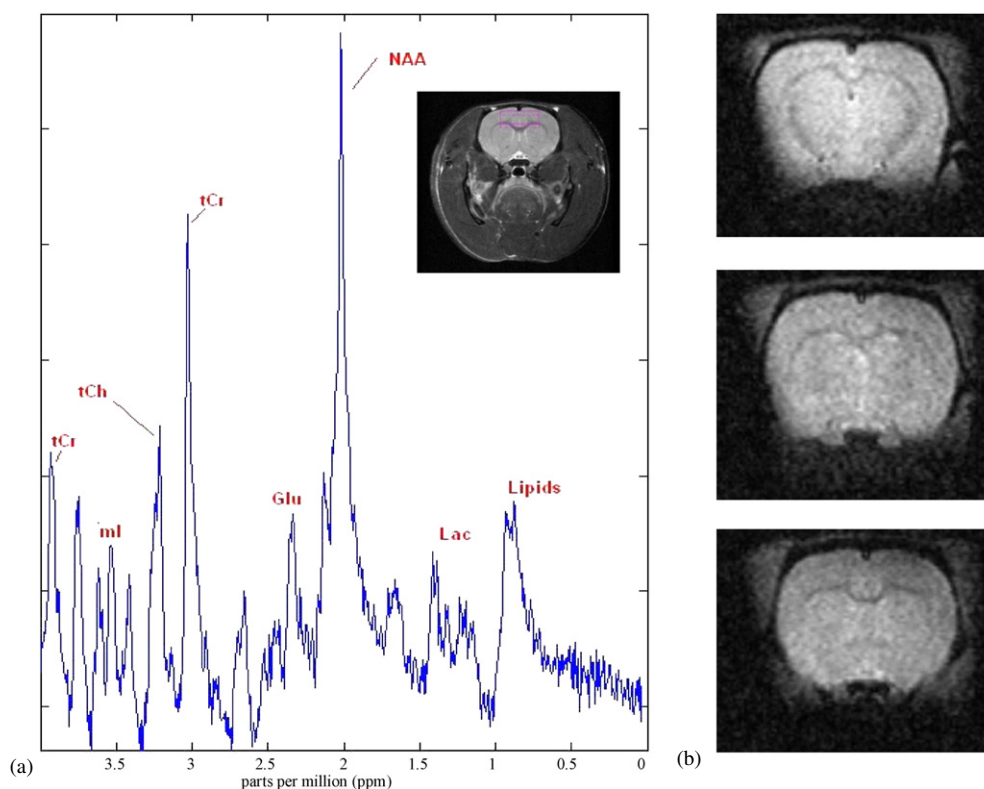


Figure 10. (a) *In vivo* MR spectrum, and (b) EPI of three transverse slices of a rat brain acquired in the presence of the PET detector.

was observed in MR images acquired with RARE sequences compared to FLASH sequences in 7 T MRI (Catana *et al* 2008). The homogeneity we recorded in the field maps obtained with the optimized shim settings is comparable both with and without the PET detector. However, we note that the shim current required for the Z2 shims was 50% higher with the PET detector than that needed for optimization without it. We attained satisfactory shims within the range of adjustments afforded by our B-GA12 Bruker gradient set and shim coil insert although the shim current we required was 97% of the maximum adjustment. The heterogeneity induced by the presence of the PET detector most likely reflects variations in the susceptibility of the components of the annular PET ring. Nevertheless, we obtained good-quality MR images throughout the active mode of PET acquisition for all the PET/MRI studies. The PET data is reproducible within 6% during the MR pulsing, even accounting for the dead time due to spurious RF pulses in the PET data. The simultaneous PET/MR images of the rat's brain show the uptake of different radiotracers. In addition, the acquisition of distortion-free EPI images and acceptably narrow spectral line-widths indicate that any distortions caused by the PET insert are correctable within the adjustment range of our set shim correction coils. Our data of the rat brain suggests that we could temporally correlate PET with MR to quantify, via MR spectra, the biodistribution of the tracer's uptake in the brain for interventional studies and tumor models. The simultaneous ECG-gated PET and MRI data on the mouse heart demonstrate our ability to acquire dynamic data allowing us to study cardiac metabolism in transgenic mice models. The metabolic information obtained from the PET then could be

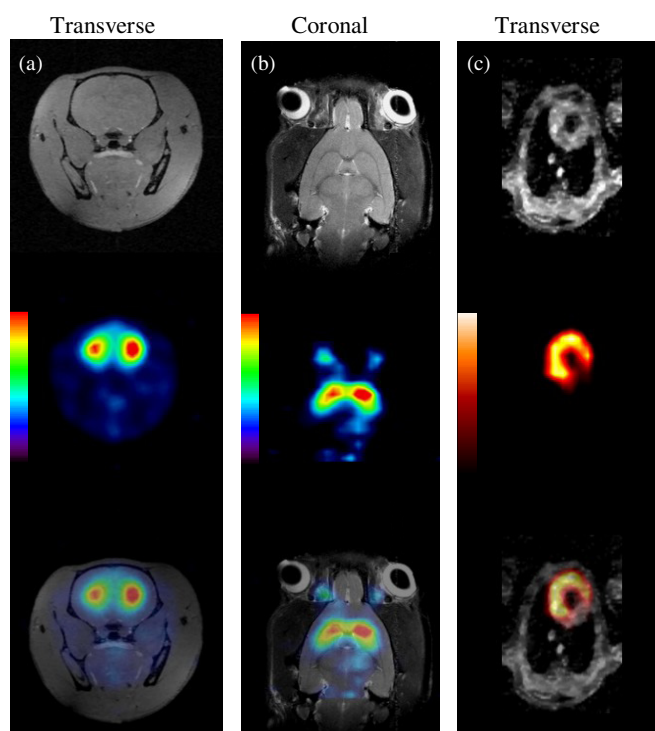


Figure 11. PET/MR images of the brain of a rat injected with [^{11}C]raclopride shows its binding to the dopamine receptor in the striatum, in the transverse view (a) acquired with the FLASH isotropic pulse, and in the coronal view (b) acquired with the RARE pulse sequence. (c) Simultaneous *cine* PET/MR-gated cardiac image of a mouse heart in transverse view showing one of the cardiac phases. The slice thickness of the MR image is matched with that of the PET image (1 mm). The images of the rat brain and mouse heart demonstrate the ability to acquire scans using the same PET/MRI setup.

correlated with the information on cardiac blood flow obtained from *cine* 3D MR images in mice models with myocardial infarction.

Although our PET detector is MRI compatible, it has a few limitations. We noted the susceptibility of the PET signal readout to the RF excitation pulses, though the functioning of the PET readout electronics was not halted permanently. The increase in the dead time in PET data stream corresponding to the duty cycle of the RF pulses is much larger (a maximum of 28%) in the RARE sequence than in the FLASH sequence (<7%). The magnitude of the noisy spikes during RARE-pulse acquisition is less for the 90° pulse than for that of the 180° refocusing pulse (figure 8(b)), reflecting the fact that less RF power is needed to flip the protons to 90° compared to the 180° pulse. The effect of RF interference on PET increases the amount of unwanted data written to the disk. Reportedly, the interference from high duty-cycle RF entailed a 20% loss in counts using SiPMs; this effect was minimized considerably by shielding the readout electronics (España *et al* 2010). No publications indicated the effect of RF interference on the PET inserts, though the effect due to the gradient switching was reported (Catana *et al* 2008). One possibility for this lack is that our MRI coil is unshielded from the PET electronics, while the standard MRI transceiver coils in some other PET/MRI systems (Wu *et al* 2009, Wehrl *et al* 2010) are well shielded. This minimizes the coupling due to the stray fields in the magnet, in addition to shielding the PET electronics. Moreover,

the sensitive detector-readout electronics for other PET/MRI systems are farther from the MRI FOV and therefore, less affected. Other factors may explain the differences between our system and others, such as readout designs, scanner geometries, MR pulse-acquisition protocols, use of optical-fiber bundles, and placements of the PET detector shielding. One reason why we did not install metallic shielding around the PET detector is that we wanted to obtain MR images with minimal attenuation of the RF power. Thus, the continuous shielded metallic enclosure in our previous PET/MRI work in 4 T MRI caused a significant reduction in the SNR, and required us to increase the power levels of the RF amplifiers (Solis *et al* 2008). The challenge is to shield the RF excitation pulses generated by the MRI coil from the PET detector electronics that are sited within 20 mm radially from the coil. With such closeness (MRI coil ID/PET ID = 32 mm/38 mm), the unshielded PET readout electronics becomes even more susceptible to RF. We carefully optimize the shielding in our PET/MRI setup and plan further to evaluate EMI effects on either one of the scanners. Reportedly, thin sheets of copper suffice to shield the PET detectors from EMI, without compromising on the quality of the MR image (Judenhofer *et al* 2007, Wu *et al* 2009, Wehrl *et al* 2010). New studies reported of the impact of a PET insert on MR imaging (Peng *et al* 2010) and that of MR hardware equipment on PET reconstruction (Delso *et al* 2010); they are of considerable interest for PET/MRI systems for evaluating the electromagnetic interactions in the MRI scanner. For our studies, we must build a complete Faraday cage around the entire PET detector using thin sheets of segmented copper to attenuate the RF generated by the MRI coil.

To our knowledge, this is the first demonstration of the flexibility that allows us to obtain PET/MRI data from the rat's brain and the mouse's heart using the same PET detector inside a high field 9.4 T MRI scanner. Others collected good quality simultaneous PET/MR images of the rat's brain (Raylman *et al* 2006, Imaizumi *et al* 2009, Yamamoto *et al* 2010). Furthermore, different groups reported quantitative mouse PET/MRI data (Catana *et al* 2008, Judenhofer *et al* 2008, Buscher *et al* 2010). We have experiments underway to evaluate the shielding configuration for our PET detectors during MRI acquisition (Maramraju *et al* 2008a, 2008b) using segmented copper layers, thereby minimizing the effects of eddy currents in the MR images and shielding the RF pulses from the PET detector electronics. This work will follow our thorough evaluation of the detector's performance inside the magnet and our identifying acceptable shield configurations to obtain PET/MRI data with minimal interference.

5. Conclusion

We demonstrated that we can obtain simultaneous PET/MR images of the brain of an adult rat and of the heart of a mouse with our MRI-compatible PET detector integrated into a 9.4 T small animal MRI scanner. Good-quality MR images of the phantoms and animals were generated with minimal interference during the PET acquisition. These initial results demonstrate the feasibility of our approach in obtaining simultaneous PET/MRI data; we will further assess shielding approaches so to undertake *in vivo* quantitative PET/MRI studies in small animals in the 9.4 T MRI scanner. Our goal in this experiment was to obtain quantitative *in vivo* spatial and temporal information simultaneously with our PET/MRI system in small animals; our initial results demonstrated its feasibility.

Acknowledgments

The authors would like to thank William Lenz for building tube assemblies, custom-made MRI coils and the rat-head holder, Joe Gatz for building the mouse holder and Joseph Carrion

for assisting in preparing and injecting the mice. They also thank the personnel at BNL's PET center and Cyclotron for providing radioisotopes for our studies. This research was carried out at Brookhaven National Laboratory under contract DE-AC02-98CH10886 with the US Department of Energy as collaboration between BNL and the State University of New York at Stony Brook.

References

- Bindseil G A, Gilbert K M, Scholl T J, Handler W B and Chronik B A 2011 First image from a combined positron emission tomography and field-cycled MRI system *Magn. Reson. Med.*
- Boss A, Bisdas S, Kolb A, Hofmann M, Ernemann U, Claussen C D, Pfannenbergl C, Pichler B J, Reimold M and Stegger L 2010a Hybrid PET/MRI of intracranial masses: initial experiences and comparison to PET/CT *J. Nucl. Med.* **51** 1198–205
- Boss A *et al* 2010b Diffusion tensor imaging in a human PET/MR hybrid system *Invest. Radiol.* **45** 270–4
- Buscher K, Judenhofer M S, Kuhlmann M T, Hermann S, Wehrl H F, Schafers K P, Schafers M, Pichler B J and Stegger L 2010 Isochronous assessment of cardiac metabolism and function in mice using hybrid PET/MRI *J. Nucl. Med.* **51** 1277–84
- Catana C, Prociassi D, Wu Y, Judenhofer M S, Qi J, Pichler B J, Jacobs R E and Cherry S R 2008 Simultaneous *in vivo* positron emission tomography and magnetic resonance imaging *Proc. Natl Acad. Sci. USA* **105** 3705–10
- Catana C, Wu Y, Judenhofer M S, Qi J, Pichler B J and Cherry S R 2006 Simultaneous acquisition of multislice PET and MR images: initial results with a MR-compatible PET scanner *J. Nucl. Med.* **47** 1968–76
- Delso G, Martinez-Moller A, Bundschuh R A, Ladebeck R, Candide Y, Faul D and Ziegler S I 2010 Evaluation of the attenuation properties of MR equipment for its use in a whole-body PET/MR scanner *Phys. Med. Biol.* **55** 4361–74
- Doty F D, Entzminger G, Kulkarni J, Pamarthy K and Staab J P 2007 Radio frequency coil technology for small-animal MRI *NMR Biomed.* **20** 304–25
- España S, Fraile L M, Herraiz J L, Udías J M, Desco M and Vaquero J J 2010 Performance evaluation of SiPM photodetectors for PET imaging in the presence of magnetic fields *Nucl. Instrum. Methods Phys. Res. A* **613** 308–16
- Garlick P B, Marsden P K, Cave A C, Parkes H G, Slates R, Shao Y, Silverman R W and Cherry S R 1997 PET and NMR dual acquisition (PANDA): applications to isolated, perfused rat hearts *NMR Biomed.* **10** 138–42
- Gati J S, Menon R S, Ugurbil K and Rutt B K 1997 Experimental determination of the BOLD field strength dependence in vessels and tissue *Magn. Reson. Med.* **38** 296–302
- Gilbert K M, Handler W B, Scholl T J, Odegaard J W and Chronik B A 2006 Design of field-cycled magnetic resonance systems for small animal imaging *Phys. Med. Biol.* **51** 2825–41
- Grazioso R, Zhang N, Corbeil J, Schmand M, Ladebeck R, Vester M, Schnur G, Renz W and Fischer H 2006 APD-based PET detector for simultaneous PET/MR imaging *Nucl. Instrum. Methods Phys. Res. A* **569** 301–5
- Hawkes R, Lucas A, Stevick J, Llosa G, Marcatili S, Piemonte C, Del Guerra A and Carpenter T A 2007 Silicon photomultiplier performance tests in magnetic resonance pulsed fields *IEEE Nucl. Sci. Symp. Conf. Record, 2007, NSS '07* pp 3400–3
- Huang B, Law M W and Khong P L 2009 Whole-body PET/CT scanning: estimation of radiation dose and cancer risk *Radiology* **251** 166–74
- Imaizumi M, Yamamoto S, Kawakami M, Aoki M, Sugiyama E, Kanai Y, Shimosegawa E and Hatazawa J 2009 Simultaneous imaging of magnetic resonance imaging and positron emission tomography by means of MRI-compatible optic fiber-based PET: a validation study in *ex vivo* rat brain *Japan. J. Radiol.* **27** 252–6
- Judenhofer M S, Catana C, Swann B K, Siegel S B, Jung W I, Nutt R E, Cherry S R, Claussen C D and Pichler B J 2007 PET/MR images acquired with a compact MR-compatible PET detector in a 7-T magnet *Radiology* **244** 807–14
- Judenhofer M S *et al* 2008 Simultaneous PET-MRI: a new approach for functional and morphological imaging *Nat. Med.* **14** 459–65
- Junnarkar S S *et al* 2008 Next generation of real time data acquisition, calibration and control system for the RatCAP scanner *IEEE Trans. Nucl. Sci.* **55** 220–4
- Kang J, Choi Y, Hong K J, Jung J H, Hu W, Huh Y S, Lim H and Kim B-T 2010 A feasibility study of photosensor charge signal transmission to preamplifier using long cable for development of hybrid PET-MRI *Med. Phys.* **37** 5655–64
- Kriplani A, Stoll S P, Schlyer D J, Shokouhi S, Vaska P, Villanueva A Jr and Woody C L 2003 Light output measurements of LSO single crystals and 4 × 8 arrays: comparison of experiment with Monte Carlo simulations *IEEE Nucl. Sci. Symp. Conf. Record, 2003* vol 5 pp 3036–40

- Lewellen T K, Harrison R L and Vannoy S 1998 *Monte Carlo Calculations in Nuclear Medicine: Applications in Diagnostic Imaging* (Bristol: Institute of Physics Publishing) pp 77–92
- Lucas A J, Hawkes R C, Ansgore R E, Williams G B, Nutt R E, Clark J C, Fryer T D and Carpenter T A 2006 Development of a combined microPET-MR system [abstract] *Technol. Cancer Res. Treat.* **5** 337–41
- Mackewn J E, Strul D, Hallett W A, Halsted P, Page R A, Keevil S F, Williams S C R, Cherry S R and Marsden P K 2005 Design and development of an MR-compatible PET scanner for imaging small animals *IEEE Trans. Nucl. Sci.* **52** 1376–80
- Maramraju S H *et al* 2008a An MR compatible PET scanner based on RatCAP for small animal imaging at 9.4 T *IEEE Nucl. Sci. Symp. Conf. Rec.* pp 3679–82
- Maramraju S H, Schlyer D, Vaska P, Woody C, Junnarkar S, Ravindranath B, Southekal S, Smith D, Tomasi D and Lenz W 2008b Acquisition of simultaneous PET-MRI images based on RatCAP PET detector in the 9.4T MRI *J. Nucl. Med.* **49** (Suppl.) 67P (abstract)
- Mawlawi O, Pan T and Macapinlac H A 2006 PET/CT imaging techniques, considerations, and artifacts *J. Thorac. Imaging* **21** 99–110
- McElroy D P, Saveliev V, Reznik A and Rowlands J A 2007 Evaluation of silicon photomultipliers: a promising new detector for MR compatible PET *Nucl. Instrum. Methods Phys. Res. A* **571** 106–9
- Park S J, Southekal S, Purschke M, Junnarkar S S, Pratte J F, Stoll S P, Woody C L, Schlyer D J and Vaska P 2008 Digital coincidence processing for the RatCAP conscious rat brain PET scanner *IEEE Trans. Nucl. Sci.* **55** 510–5
- Peng B J, Walton J H, Cherry S R and Willig-Onwuachi J 2010 Studies of the interactions of an MRI system with the shielding in a combined PET/MRI scanner *Phys. Med. Biol.* **55** 265–80
- Pichler B J, Judenhofer M S, Catana C, Walton J H, Kneilling M, Nutt R E, Siegel S B, Claussen C D and Cherry S R 2006 Performance test of an LSO-APD detector in a 7-T MRI scanner for simultaneous PET/MRI *J. Nucl. Med.* **47** 639–47
- Poole M, Bowtell R, Green D, Pittard S, Lucas A, Hawkes R and Carpenter A 2009 Split gradient coils for simultaneous PET-MRI *Magn. Reson. Med.* **62** 1106–11
- Pratte J F *et al* 2008 The RatCAP front-end ASIC *IEEE Trans. Nucl. Sci.* **55** 2727–35
- Raylman R R, Majewski S, Lemieux S K, Velan S S, Kross B, Popov V, Smith M F, Weisenberger A G, Zorn C and Marano G D 2006 Simultaneous MRI and PET imaging of a rat brain *Phys. Med. Biol.* **51** 6371–9
- Schaart D R, Seifert S, Vinke R, van Dam H T, Dendooven P, Lohner H and Beekman F J 2010 LaBr(3):Ce and SiPMs for time-of-flight PET: achieving 100 ps coincidence resolving time *Phys. Med. Biol.* **55** N179–89
- Schick F 2005 Whole-body MRI at high field: technical limits and clinical potential *Eur. Radiol.* **15** 946–59
- Schlemmer H P *et al* 2008 Simultaneous MR/PET imaging of the human brain: feasibility study *Radiology* **248** 1028–35
- Schlyer D, Rooney W, Woody C, Vaska P, Kriplani A and Stoll S 2004 Development of a simultaneous PET/MRI scanner *IEEE Nucl. Sci. Symp. Conf. Rec.* pp 3419–21
- Schlyer D *et al* 2007 A Simultaneous PET/MRI scanner based on RatCAP in small animals *IEEE Nucl. Sci. Symp. Conf. Rec.* vol 5 pp 3256–9
- Seong Jong H, In Chan S, Ito M, Sun Il K, Geon Song L, Kwang-Souk S, Kwang Suk P, June Tak R and Jae Sung L 2008 An investigation into the use of Geiger-mode solid-state photomultipliers for simultaneous PET and MRI acquisition *IEEE Trans. Nucl. Sci.* **55** 882–8
- Shao Y, Cherry S R, Farahani K, Meadors K, Siegel S, Silverman R W and Marsden P K 1997 Simultaneous PET and MR imaging *Phys. Med. Biol.* **42** 1965–70
- Slates R B, Farahani K, Shao Y, Marsden P K, Taylor J, Summers P E, Williams S, Beech J and Cherry S R 1999 A study of artefacts in simultaneous PET and MR imaging using a prototype MR compatible PET scanner *Phys. Med. Biol.* **44** 2015–27
- Solis E, Tomasi D, Junnarkar S, Schlyer D, Vaska P, Woody C, Pratte J F, O'Connor P and Rodriguez A O 2008 Shielded transceiver RF coil array for simultaneous PET-MRI *Braz. J. Phys.* **38** 287–91
- Southekal S 2009 Strategies for quantitative neuroimaging with the rat conscious animal PET (RatCAP) *PhD Dissertation* Stony Brook University, NY
- Southekal S, Purschke M, Woody C L, Schlyer D J and Vaska P 2007 Optimization of image reconstruction for the RatCAP (PET) tomograph: an analysis of the statistical quality of the system response matrix *IEEE Nucl. Sci. Symp. Conf. Rec.* vol 4 pp 3051–4
- Sureshbabu W and Mawlawi O 2005 PET/CT imaging artifacts *J. Nucl. Med. Technol.* **33** 156–61
- Tkac I, Henry P G, Andersen P, Keene C D, Low W C and Gruetter R 2004 Highly resolved *in vivo* ¹H NMR spectroscopy of the mouse brain at 9.4 T *Magn. Reson. Med.* **52** 478–84
- Toi V *et al* 2010 Challenges and opportunities of ultra-high field MRI *The Third International Conference on the Development of Biomedical Engineering in Vietnam* ed R Magjarevic (Berlin: Springer) pp 1–5

- Vaska P *et al* 2004 RatCAP: miniaturized head-mounted PET for conscious rodent brain imaging *IEEE Trans. Nucl. Sci.* **51** 2718–22
- Vaska P *et al* 2007 The design and performance of the 2nd-generation RatCAP awake rat brain PET system *IEEE Nucl. Sci. Symp. Conf. Rec.* vol 6 pp 4181–4
- Wehrl H F, Judenhofer M S, Thielscher A, Martirosian P, Schick F and Pichler B J 2010 Assessment of MR compatibility of a PET insert developed for simultaneous multiparametric PET/MR imaging on an animal system operating at 7 T *Magn. Reson. Med.* **65** 269–79
- Woody C *et al* 2004 The RatCAP conscious small animal PET tomograph *IEEE Nucl. Sci. Symp. Conf. Rec., 2004* vol 4 pp 2334–8
- Woody C *et al* 2007a Preliminary studies of a simultaneous PET/MRI scanner based on the RatCAP small animal tomograph *Nucl. Instrum. Methods Phys. Res. A* **571** 102–5
- Woody C *et al* 2007b Initial studies using the RatCAP conscious animal PET tomograph *Nucl. Instrum. Methods Phys. Res. A* **571** 14–7
- Wu Y, Catana C, Farrell R, Dokhale P A, Shah K S, Jinyi Q and Cherry S R 2009 PET performance evaluation of an MR-compatible PET insert *IEEE Trans. Nucl. Sci.* **56** 574–80
- Yamamoto S, Imaizumi M, Kanai Y, Tatsumi M, Aoki M, Sugiyama E, Kawakami M, Shimosegawa E and Hatazawa J 2010 Design and performance from an integrated PET/MRI system for small animals *Ann. Nucl. Med.* **24** 89–98